



# Oxidation promoted osmotic energy conversion in black phosphorus membranes

Zhen Zhang<sup>a,b</sup>, Panpan Zhang<sup>a,b</sup>, Sheng Yang<sup>a,b</sup>, Tao Zhang<sup>a,b</sup>, Markus Löffler<sup>c</sup>, Huanhuan Shi<sup>a,b</sup>, Martin R. Lohe<sup>a,b</sup>, and Xinliang Feng<sup>a,b,1</sup>

<sup>a</sup>Center for Advancing Electronics Dresden, Technische Universität Dresden, 01062 Dresden, Germany; <sup>b</sup>Faculty of Chemistry and Food Chemistry, Technische Universität Dresden, 01062 Dresden, Germany; and <sup>c</sup>Dresden Center for Nanoanalysis, Center for Advancing Electronics Dresden, Technische Universität Dresden, 01062 Dresden, Germany

Edited by Alexis T. Bell, University of California, Berkeley, CA, and approved May 11, 2020 (received for review March 6, 2020)

**Two-dimensional (2D) nanofluidic ion transporting membranes show great promise in harvesting the “blue” osmotic energy between river water and sea water. Black phosphorus (BP), an emerging layered material, has recently been explored for a wide range of ambient applications. However, little attention has been paid to the extraction of the worldwide osmotic energy, despite its large potential as an energy conversion membrane. Here, we report an experimental investigation of BP membrane in osmotic energy conversion and reveal how the oxidation of BP influences power generation. Through controllable oxidation in water, power output of the BP membrane can be largely enhanced, which can be attributed to the generated charged phosphorus compounds. Depending on the valence of oxidized BP that is associated with oxygen concentration, the power density can be precisely controlled and substantially promoted by ~220% to 1.6 W/m<sup>2</sup> (compared with the pristine BP membrane). Moreover, through constructing a heterostructure with graphene oxide, ion selectivity of the BP membrane increases by ~80%, contributing to enhanced charge separation efficiency and thus improved performance of ~4.7 W/m<sup>2</sup> that outperforms most of the state-of-the-art 2D nanofluidic membranes.**

nanofluidics | black phosphorus | ion transport | osmotic energy

**S**olution-dispersed two-dimensional (2D) materials can be readily assembled into ultrathin paper-like membranes with massive interconnected and highly uniform interstitial channels, enabling tunable nanoconfinement from a few nanometers down to the subnanometer level, termed 2D nanofluidic membranes (1). The transport of electrolytes and water in such narrow channels can be significantly different from that in the bulk. When the size of the interlayer channel is close to the Debye length, the ion transport process will be fully dominated by the surface charge that is associated with the surface chemistry of the constituent material (2). Diverse exciting phenomena such as ultrafast permeation and highly selective transport have been found in 2D nanofluidic membranes consisting of, for example, graphene, molybdenum disulfide, boron nitride, and other atomically thin materials (3–8). These discoveries provide unprecedented insights into the structure–property relationships of 2D confined transport process and have shown promising prospects in many areas such as molecular/ionic sieving (9–12) and osmotic energy conversion (13–18) (namely the extraction of power from the mixing of sea water and river water).

Black phosphorus (BP), the most stable allotrope of elemental phosphorus, has emerged as a new type of layered materials and attracted growing interest in the scientific community due to its distinguishing virtues such as highly anisotropic charge-transport and thickness-tunable bandgaps (0.3–2 eV) (19–21). Layered BP is prone to oxidize when exposed to the ambient environment (22–24). In field-effect transistors, the oxidation will sharply decrease the on/off ratio and charge carrier mobility, and the demonstration must be conducted under the protection of inert gas or through applying complicated surface passivation techniques (25, 26). In the past years, BP and oxidized BP have been explored for a wide range of ambient applications such as sensing

and energy storage (23, 27–33). For example, the fast and reversible pseudocapacitive behavior of BP nanosheets with molecular-level redox-active P=O sites is reported, and the observed surface redox pseudocapacitance exceeds the kinetic limitations (28). Also, BP composite nanosheets are demonstrated as promising anode materials for lithium and sodium-ion batteries, exhibiting high reversible capacities (29, 30). With respect to the osmotic energy conversion, the emerging BP can be an excellent candidate because its hydrophilic nature and net charge provided by the oxidized sites will largely promote the ionic separation in confined channels (34, 35).

Here we report an experimental investigation of BP membrane that is fabricated by assembling the exfoliated nanosheets in osmotic energy conversion and reveal how the oxidation of BP influences the power generation (Fig. 1A). The coexistence of O<sub>2</sub> and water can contribute to oxidation of BP, generating charged phosphorus compounds with controllable valence positively correlated with oxygen concentration. During the energy conversion process, the high-valence phosphorus (V) compound delivers more negative charge than the low-valence ones, contributing to a maximum 220% increase of power density from 0.5 to 1.6 W/m<sup>2</sup> (compared with a pristine sample). Furthermore, multilayer graphene oxide (GO)-intercalated BP membrane is constructed by adopting a nature-inspired design coming from the soil. The introduction of multilayer structure largely increases the ion selectivity, contributing to enhanced charge separation efficiency, as

## Significance

Engineering two-dimensional (2D) membranes has been an effective approach to boost the harvesting of the “blue” osmotic energy between river water and sea water. Here we show the oxidation of black phosphorus (BP) can be fully utilized for osmotic energy conversion, which stands in contrast to using BP for electronic applications where the ambient stability is a major concern. Through controllable oxidation in water, power output of the BP membrane can be largely promoted by ~220% to 1.6 W/m<sup>2</sup>. Moreover, construction of a heterostructure membrane with graphene oxide greatly enhances the charge separation efficiency, contributing to improved performance of ~4.7 W/m<sup>2</sup> that outperforms most of the 2D membranes. This work highlights BP as an attractive material for nanofluidic energy conversion.

Author contributions: Z.Z. and X.F. designed research; Z.Z., P.Z., S.Y., T.Z., and H.S. performed research; Z.Z., S.Y., M.L., M.R.L., and X.F. analyzed data; and Z.Z. and X.F. wrote the paper.

The authors declare no competing interest.

This article is a PNAS Direct Submission.

Published under the PNAS license.

<sup>1</sup>To whom correspondence may be addressed. Email: xinliang.feng@tu-dresden.de.

This article contains supporting information online at <https://www.pnas.org/lookup/suppl/doi:10.1073/pnas.2003898117/-DCSupplemental>.

First published June 8, 2020.

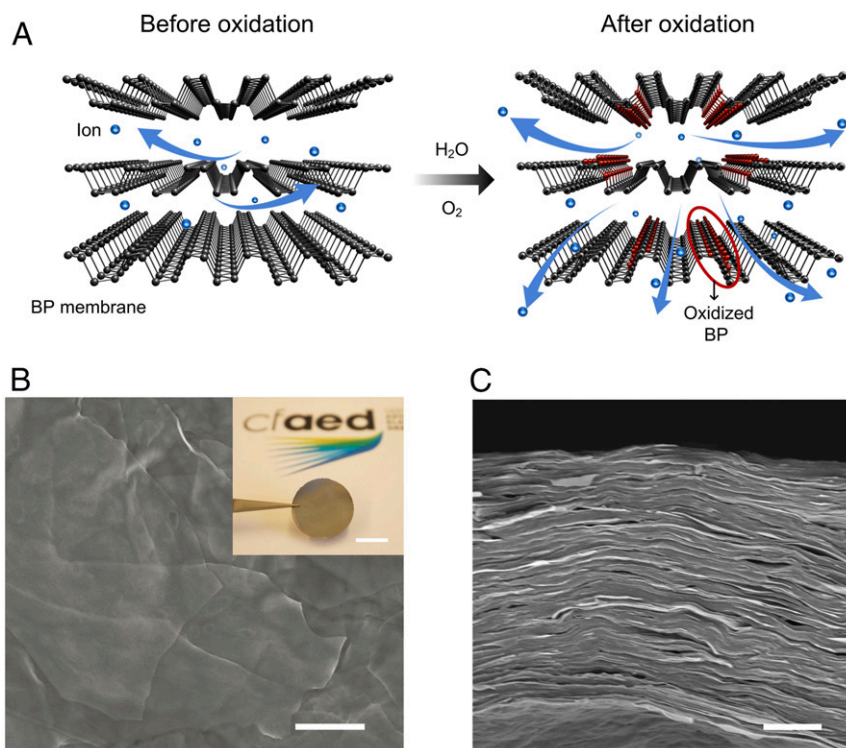


**Fig. 1.** BP membrane made from exfoliated nanosheets. (A) The coexistence of water and  $O_2$  contributes to the oxidation of BP, generating functional phosphorus compounds (red circle). These compounds can serve as charged sites in electrolyte solution, accelerating the transmembrane ion transport and eventually promoting the osmotic energy conversion. (B) Surface SEM image of the as-prepared BP membrane. (Scale bar, 1  $\mu\text{m}$ .) (Inset) A free-standing BP membrane fabricated by the vacuum filtration method. (Scale bar, 1 cm.) (C) Cross-section SEM images of the BP membrane. (Scale bar, 2  $\mu\text{m}$ .)

evidenced by a 64~95% increase of osmotic potential depending on the number of GO layers. Improved power density of  $\sim 4.7 \text{ W/m}^2$  with natural sea-water pair is achieved, outperforming most of the reported 2D nanofluidic membranes. This work highlights the large potential of BP in surface-charge-governed aqueous nanofluidic energy devices.

## Results

**Fabrication and Characterization of the BP Membrane.** Thinly layered defect-free BP nanosheets were prepared by the electrochemical delamination strategy developed by our group (*SI Appendix, Fig. S1*) (36). The as-prepared nanosheets exhibit a few-layer structure with average size  $\sim 1.5 \mu\text{m}$  (*SI Appendix, Figs. S2–S4*). Through a vacuum-filtration method, the BP nanosheets can be readily reconstructed into a free-standing membrane (Fig. 1B). Surface scanning electron microscope (SEM) images reveal that the as-prepared membrane is stacked densely by ultrathin 2D nanosheets with observable interstitial space. Large-area lattice fringes of (040) plane with space distance of  $\sim 2.6 \text{ \AA}$  are observed in the high-resolution transmission electron microscope image of the constituent nanosheet, indicating that the membrane is composed of highly crystalline BP (*SI Appendix, Fig. S5*). The BP membrane shows a typical lamellar microstructure with a thickness of about  $8 \mu\text{m}$  (Fig. 1C). The macroscopic membrane is stable in water. After being immersed in water for 3 months, it still remains intact and there are no observable morphological changes (*SI Appendix, Fig. S6*).

**Nanofluidic Ion Transport through the BP Membrane.** Fig. 2A shows X-ray diffraction (XRD) analysis of the BP membrane and bulk BP crystal. Because of the presence of few-layer BP, characteristic peaks of highly crystalline BP centered at around  $17.0^\circ$  (020),  $34.3^\circ$  (040), and  $52.5^\circ$  (060) are observed in the membrane

sample (Fig. 2A, *Inset*). Different from bulk crystal, a single peak emerges in the low-angle region ( $\sim 9.2^\circ$ ) in the BP membrane, revealing the uniform structure of the membrane with an interlayer spacing of  $4.4 \text{ \AA}$  (after subtraction of single-layer thickness) (*SI Appendix, Note S1 and Fig. S7*). This means that the BP membrane could act as an ion transport medium but not a barrier (37). The ion transport behavior was investigated by clamping the BP membrane in a two-compartment electrochemical cell (Fig. 2B and *SI Appendix, Fig. S8*) (38). A pair of Ag/AgCl electrodes was used to record the transmembrane ionic current. Representative current–voltage ( $I$ – $V$ ) curves at various KCl electrolyte concentrations are shown in Fig. 2C. The measured ionic current is in the microampere regime, which is larger than that in the track-etched polymer membrane (39), indicating the good ion transport ability of the BP membrane. All of the current responses exhibit linear ohmic behavior with negligible ionic diode effect, which are typical characteristics for nanofluidic membranes with symmetric microstructure.

The ionic conductance exhibits a distinct relationship with the concentration of the electrolyte. As shown in Fig. 2D, the measured conductance gradually deviates from bulk value (red dashed line). In general, the conductance of a nanofluidic channel filled with electrolyte solution is composed of two parts: bulk conductance contributed by the bulk electrolyte ( $G_{\text{bulk}}$ ) and surface conductance contributed by the surface charge ( $G_{\text{surface}}$ ) (40, 41):

$$G = G_{\text{bulk}} + G_{\text{surface}} = (u_+ + u_-)cN_A e w d / l + 2u_+ \sigma_s w / l,$$

where  $u_+$  and  $u_-$  are mobility of cation and anion, respectively;  $c$  is the concentration of bulk solution;  $N_A$  is Avogadro's number;  $e$  is the elementary charge;  $d$  is the free interlayer spacing;  $w$  and  $l$  are the width and length of the channel, respectively; and  $\sigma_s$  is

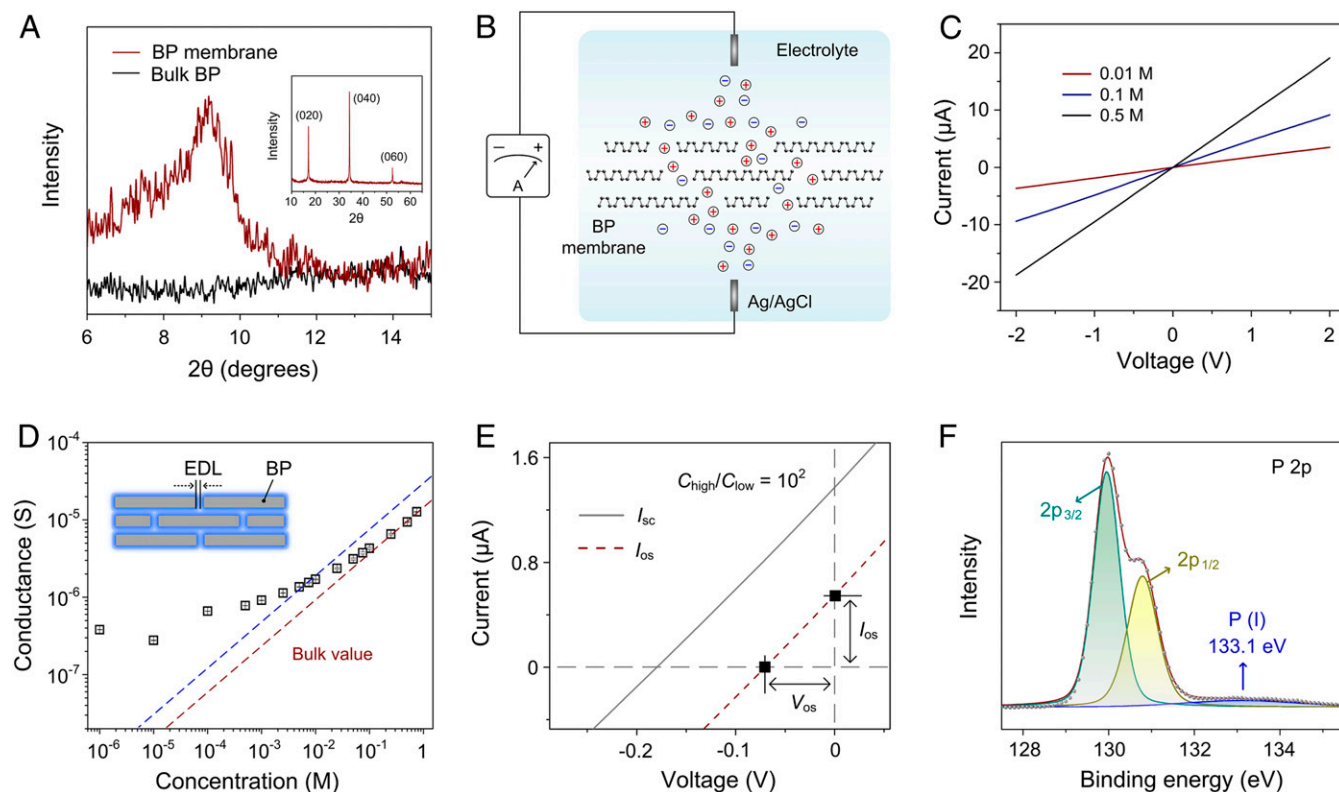


**Fig. 2.** Nanofluidic ion transport through the BP membrane. (A) XRD analysis of the BP membrane and bulk BP crystal in the low-angle region. (Inset) The characteristic XRD crystalline peaks observed in the BP membrane. (B) Schematic of the vertical ion transport across the BP membrane. (C) Current-voltage curves of the BP membrane recorded in KCl electrolyte with different concentrations. (D) Transmembrane ionic conductance as a function of electrolyte concentration, which gradually deviates from bulk value (red dash line), indicating a surface-charge-governed ion transport. The blue dashed line represents double bulk value and the surface charge density is estimated to be  $0.25 \text{ mC/m}^2$ . EDL denotes the electric double layer. (E) Current-voltage curve (solid line) of the BP membrane under a 100-fold KCl concentration ( $C_{\text{high}} = 1 \text{ M}$ ,  $C_{\text{low}} = 0.01 \text{ M}$ ). The contribution from the redox potential has been subtracted, generating the dashed line that represents the pure osmotic contribution. (F) P 2p XPS spectrum of the BP membrane.

the surface charge density (42). The bulk conductance (left term) governs the measured ionic conductance in the high-concentration region, whereas in the low-concentration region the electric double layers overlap and the contribution from surface (right term) plays a predominant role. The experimentally observed deviation reveals that the ion transport in BP membrane is governed by the surface charges (43–45). The surface charge of the pristine BP membrane is estimated to be  $\sim 0.25 \text{ mC/m}^2$  (*SI Appendix, Note S2*), which is much lower than the values ( $1\text{--}2 \text{ mC/m}^2$ ) of conventional 2D materials such as GO (40), clay (43), and boron nitride (5).

*I-V* measurement was also performed under a 100-fold KCl transmembrane concentration gradient, which exhibited obvious intercepts on the coordinate axis (i.e., open-circuit voltage and short-circuit current; Fig. 2E, solid line). The pure osmotic potential ( $V_{\text{os}}$ ) and current ( $I_{\text{os}}$ ) can be extracted by subtracting the contribution of redox potential on the electrode, generating the dashed line. Note that the direction of the obtained  $I_{\text{os}}$  is consistent with the net flow of cations from the high-concentration to the low-concentration side, implying the cation selectivity of the BP membrane. Accordingly, the transference number of the cation can be quantified by the  $V_{\text{os}}$  through the following equation:

$$V_{\text{os}} = (t_+ - t_-) \frac{RT}{F} \ln \left[ \frac{a_{\text{high}}}{a_{\text{low}}} \right],$$

where,  $t_+$  and  $t_-$  are the transference numbers for cations and anions respectively.  $R$ ,  $T$ ,  $F$ , and  $a$  are the universal gas constant,

the absolute temperature, the Faraday constant, and the activities of electrolyte, respectively. Here, the cation transference number of the BP membrane is calculated to be  $\sim 0.83$ . The observed deviation of ionic conductance and selectivity of cations both confirm the existence of surface charges in the BP membrane. The net charge can be ascribed to the oxidation of BP during the membrane fabrication process, which creates multitypes of charged compounds (25). As characterized by high-resolution X-ray photoelectron spectroscopy (HRXPS) (Fig. 2F), in addition to the strong characteristic peaks of crystalline BP at  $\sim 130 \text{ eV}$  ( $2p_{3/2}$ ) and  $\sim 131 \text{ eV}$  ( $2p_{1/2}$ ), subbands at around  $133.1 \text{ eV}$  are observed, attributable to the low-valence phosphorus (I) oxidized compounds.

**Oxidation Promoted Osmotic Energy Conversion.** To evaluate the osmotic energy conversion behavior, the BP membrane was placed between a standard concentration gradient of simple inorganic salt that simulates natural river water and sea water (i.e.,  $0.01 \text{ M}/0.5 \text{ M}$  NaCl) and then connected to an external circuit containing an adjustable external load ( $R_L$ ). As shown in Fig. 3A, the current density on the external circuit decreases with increasing resistance. The output power density, calculated as  $P = I^2 \times R_L$ , achieves a maximum value of about  $0.5 \text{ W/m}^2$  at an intermediate resistance ( $R_m$ ) of  $\sim 250 \text{ k}\Omega$ . The corresponding energy conversion efficiency is calculated to be 14% (*SI Appendix, Note S3 and Fig. S9*) (46). Next, we found that the subsequent treatment of the BP membrane through water immersion could largely increase the power output (Fig. 3B). In



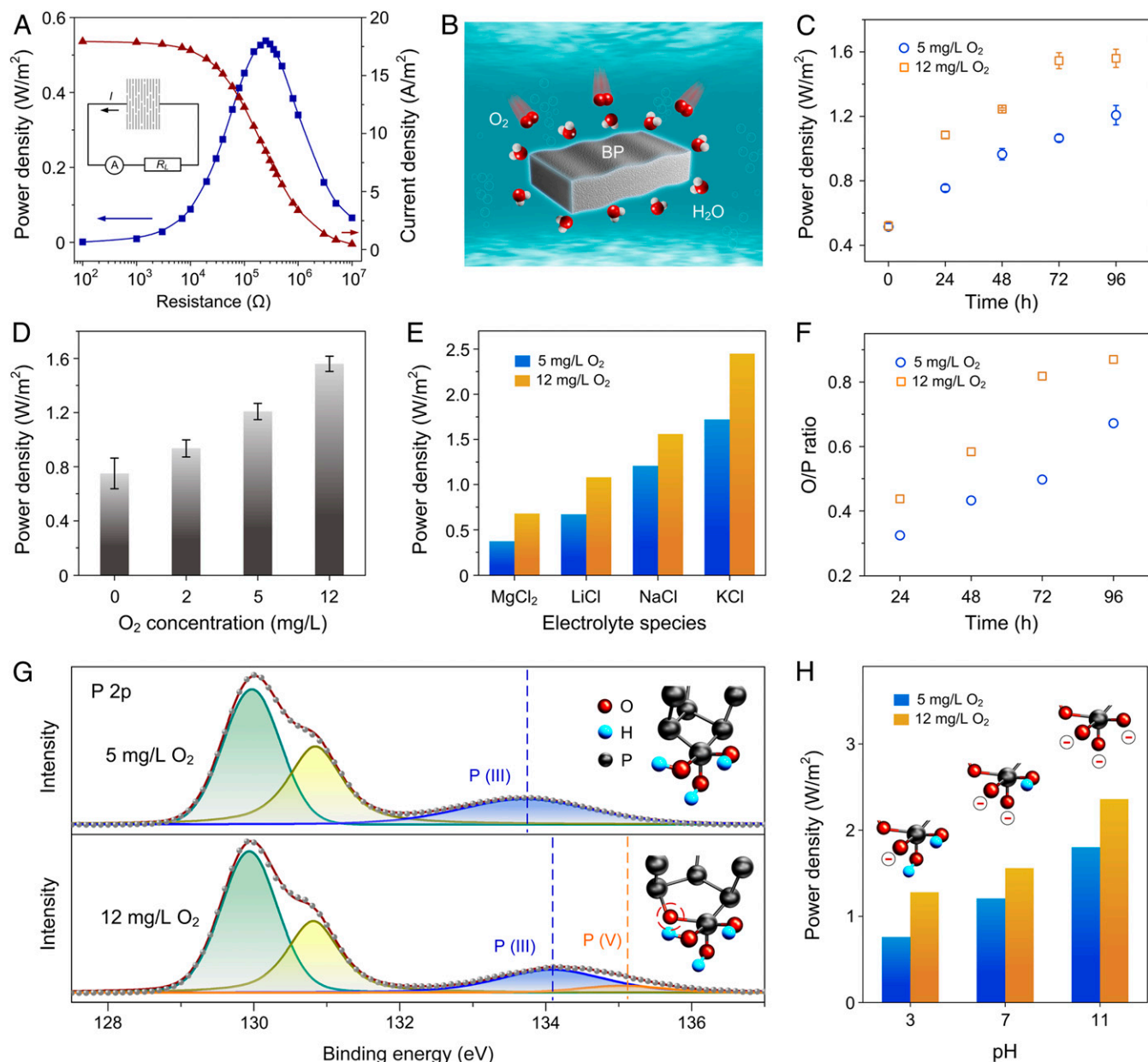


**Fig. 3.** Oxidation promoted osmotic energy conversion. (A) Power output of the BP membrane under 0.5 M/0.01 M NaCl salinity gradient. (B) Schematic of the treatment of BP membrane: immersed in  $\text{O}_2$ -containing water. (C) Output power densities as a function of water treatment time under high (12 mg/L) and normal (5 mg/L)  $\text{O}_2$  concentration. (D) Output power density as a function of  $\text{O}_2$  concentration. (E) Output power density as a function of electrolyte species. (F) Oxidation degree (quantified by the atomic ratio of O and P elements) as a function of water treatment time, showing good agreement with the variation of power densities in C. (G) P 2p XPS spectra of the BP membrane after water treatment under 5 mg/L and 12 mg/L  $\text{O}_2$  concentration condition. (Inset) The most stable structure of oxidized P (III) and P (V) compounds that both carry three hydroxyl groups. (H) Influence of the pH of the electrolyte on the output power density. (Inset) The gradual dissociation of P-OH groups.

normal deionized (DI) water with  $\text{O}_2$  concentration  $\sim 5 \text{ mg/L}$ , the power density increases gradually from  $0.5 \text{ W/m}^2$  to  $1.2 \text{ W/m}^2$  upon increasing the immersion time to 96 h (Fig. 3C), while in the  $\text{O}_2$ -bubbled water ( $\sim 12 \text{ mg/L}$ ) the delivered power density is much larger but levels off after 72 h to  $\sim 1.6 \text{ W/m}^2$ . The power output of the BP membrane shows a linear relationship with the  $\text{O}_2$  concentration in water (Fig. 3D). By contrast, BP membrane placed in air for the same time period shows negligible increase of the power density (SI Appendix, Fig. S10). These observations indicate that the  $\text{O}_2$  and water both play irreplaceable roles in the performance enhancement

of the BP membrane. Besides NaCl, the BP membrane after water treatment is also capable of harvesting osmotic energy from diverse types of electrolyte (Fig. 3E). As the membrane is cation-selective, the faster the cation diffuses, the more remarkable the charge separation that will occur, resulting in the highest power output in KCl electrolyte ( $\sim 2.5 \text{ W/m}^2$ ) (47).

Previous reports have shown that the coexistence of  $\text{O}_2$  and water can accelerate the oxidation of BP (22, 24). When oxygen coadsorbs with highly polarized water molecules on the BP surface, the energy levels of oxygen will be lowered due to the polarization effect of water, greatly facilitating the electron

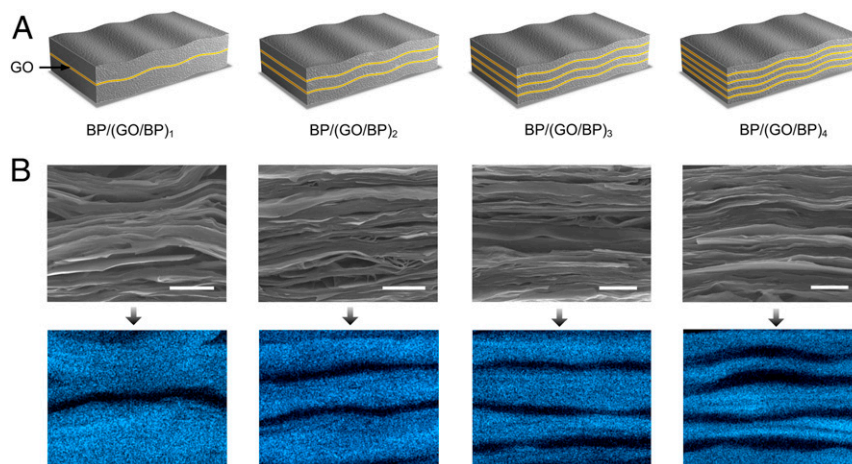
transfer from BP to oxygen (22). Therefore, we speculate that such a pronounced enhancement in the power generation could be ascribed to the enhanced oxidation of BP membrane, which can create more charged surface functional groups and eventually promote the osmotic energy conversion (48). Nevertheless, no morphological changes were observed in the SEM images, even after keeping for 10 d (*SI Appendix, Fig. S11*), indicating that the oxidation mainly occurred in the nanoscale domains. The degree of oxidation can be quantified by the atomic ratio of O and P elements (i.e., O/P ratio characterized by XPS). As shown in Fig. 3*F*, the O/P ratio under normal O<sub>2</sub> concentration conditions ( $\sim 5$  mg/L) increases gradually from 0.32 to 0.67 upon the prolonged treatment from 24 to 96 h, while the measured ratio under high O<sub>2</sub> concentration conditions ( $\sim 12$  mg/L) is much larger and increases from 0.44 to 0.87. These changes are in good agreement with the variation of power densities (Fig. 3*C*).

Fig. 3*G* shows the HRXPS results of the BP membranes after 96-h water treatment. Under 5 mg/L O<sub>2</sub> concentration condition, compared with the pristine BP membrane, the intensity of the subband increases substantially, and the binding energy increases from 133.1 to 133.7 eV, which corresponds to the increase of the valence of the phosphorus compounds from P (I) to P (III). Under high-concentration conditions (12 mg/L), the binding energy of P (III) shifts to a higher level  $\sim 134.1$  eV, and another peak at about 135.1 eV emerges, implying the formation of high valence (V) phosphorus compound. The most stable structures of the compounds of the P (III) and P (V) on BP's surface have both been proven to carry three hydroxyl (-OH) groups (Fig. 3*G, Inset*) (49). With regard to the P (V) compound, the extra oxygen atom (highlighted by a dashed circle) with high electronegativity makes the -OH groups much easier to deprotonate to carry negative charges than those of P (III) compound. The surface charge density is estimated to be 2 mC/m<sup>2</sup> in the existence of P (V) compound that is higher than the case of P (III) compound ( $\sim 1$  mC/m<sup>2</sup>), thus enabling larger power density under high O<sub>2</sub> concentration conditions (*SI Appendix, Fig. S12*). The pH value of electrolyte solution has a strong influence on the osmotic energy conversion property. As shown in Fig. 3*H*, under 5 mg/L O<sub>2</sub> concentration conditions, the power density of BP membrane increases from 0.76 to 1.8 W/m<sup>2</sup> upon increasing the pH from 3 to 11, while under 12 mg/L O<sub>2</sub> concentration conditions the power density is much larger and increases from 1.2 to 2.8 W/m<sup>2</sup>. These observations can be ascribed to the gradual dissociation of

phosphorus compound (i.e., increase of surface charge) upon varying the pH value.

**Improved Osmotic Energy Conversion in Multilayer BP Composite Membrane.** In order to enhance the performance of BP membrane to commercially attractive values, we further constructed multilayer BP composite membranes which were prepared by controllably intercalating GO layers within the BP membrane. Such a membrane design takes inspiration from the multilayer architecture in nature (for example, soil that consists of different horizons such as gravel and sand with varying fluidic transport routes) (50). In this work, the multilayer membrane was prepared by sequential filtration of BP and GO dispersion (*Materials and Methods* and *SI Appendix, Figs. S13 and S14*), and the top and bottom layers were both BP membranes. The thickness of every single GO layer is set to  $\sim 500$  nm and the total thickness of the composite membrane is uniformly set to  $\sim 8$   $\mu$ m, the same as the pristine BP membrane. According to the number (*n*) of the layer of GO membrane, the intercalated BP membrane is defined as BP/(GO/BP)<sub>*n*</sub> (Fig. 4*A*). Fig. 4*B* shows the cross-section SEM images of a series of composite membranes (*n* = 1, 2, 3, and 4) and the corresponding energy dispersive X-ray (EDX) mapping of phosphorus element. All of the membranes exhibit typical lamellar microstructure and the alternately stacked BP layer (blue stripe) and GO layer (black stripe) can be clearly distinguished.

The composite membranes show substantially enhanced ability in harvesting the osmotic energy existing between a trans-membrane ionic concentration gradient (Fig. 5*A*). Fig. 5*B* presents the power output of BP/(GO/BP)<sub>3</sub> membrane before and after treatment using oxygenated water (12 mg/L). The power density of pristine BP/(GO/BP)<sub>3</sub> membrane ( $\sim 0.76$  W/m<sup>2</sup>) is larger than that of the pristine BP membrane ( $\sim 0.5$  W/m<sup>2</sup>). The subsequent water treatment contributes to  $\sim 350\%$  increase of power density from 0.76 to 3.4 W/m<sup>2</sup>, which can be ascribed to the introduction of multilayer architecture in combination with the increased surface charge resulting from oxidation. Contrast experiments were also performed with composite membrane having the same weight ratio prepared by the commonly used method, namely one-step filtration of the mixture of colloidal dispersions of BP and GO. As shown in Fig. 5*C*, the power density of the composite membrane prepared through simple mixing is  $\sim 2.5$  W/m<sup>2</sup> (*SI Appendix, Fig. S15*); this value is much lower than that of the sequentially assembled composite



**Fig. 4.** Controllable intercalation of GO layer. (A) Schematic of four intercalated BP membranes with increasing number of GO membranes (*n* = 1, 2, 3, and 4). (B) Cross-section SEM images and the corresponding EDX mapping of phosphorus element. (Scale bars, 2.5  $\mu$ m.) The blue stripes represent the BP layer and the black stripes represent the GO layer.

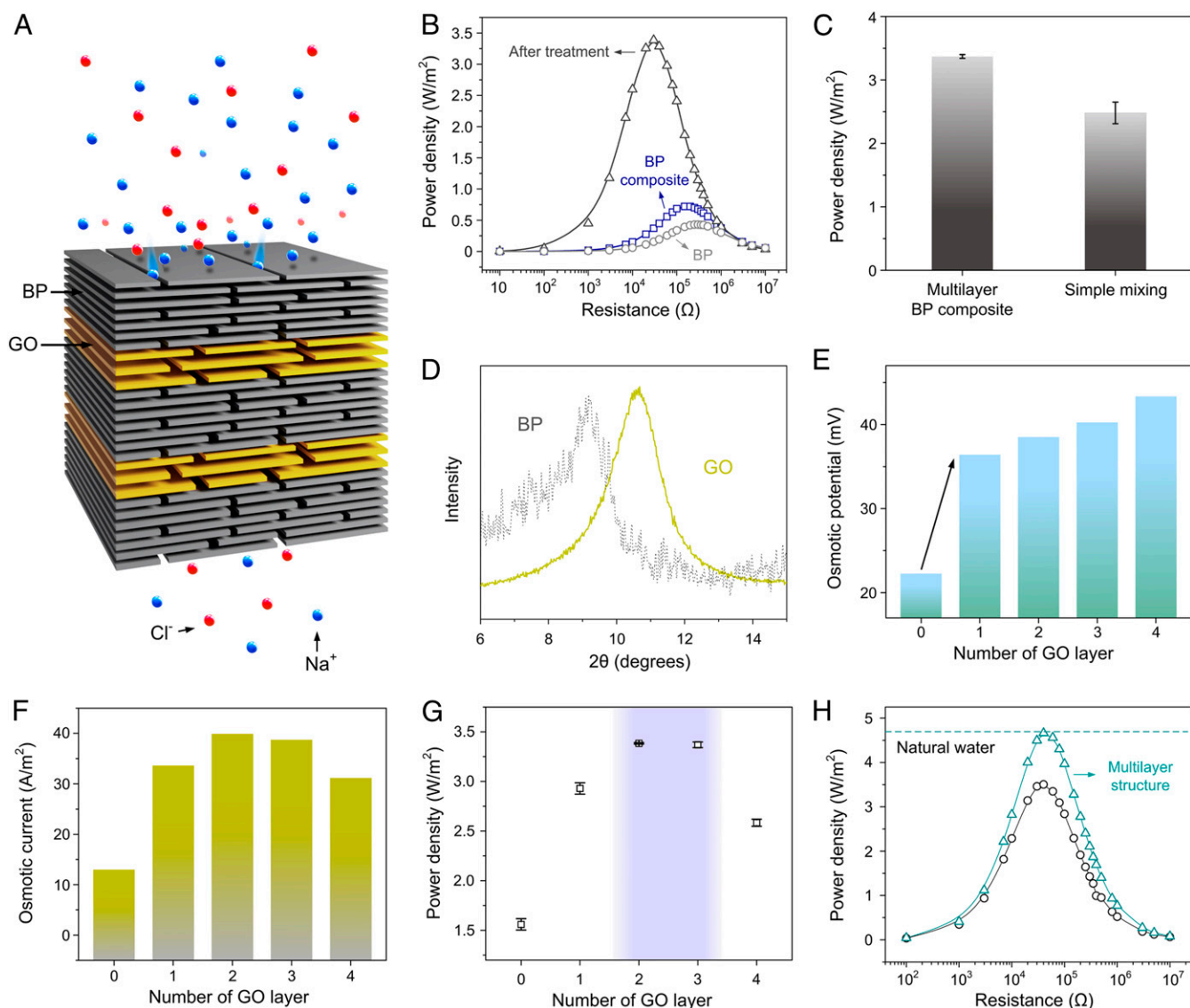


**Fig. 5.** Improved osmotic energy conversion in multilayer BP composite membrane. (A) Schematic of the transmembrane ion transport of the multilayer membrane under a concentration gradient. (B) Power output of BP/(GO/BP)<sub>3</sub> membrane before (square) and after (triangle) being immersed in water with O<sub>2</sub> concentration of 12 mg/L for 96 h. The power out of pristine BP membrane is plotted for comparison (circle). (C) Comparison of the power density of BP/(GO/BP)<sub>3</sub> membrane with the composite membrane of the same weight ratio prepared through simple mixing of BP and GO. (D) XRD pattern of GO membrane (solid line). The XRD result of BP membrane is also plotted for direct comparison (dashed line). After subtraction of single-layer thickness, the GO membrane exhibits a larger interlayer channel (~5 Å) than the BP membrane (~4 Å). (E–G) Influence of number of layers of GO on the osmotic potential (E), osmotic current (F), and the overall power density (G). (H) Energy conversion behavior of the composite membranes fabricated through sequential assembly (triangle) and simple mixing (circle) under the concentration gradient of natural sea water and river water.

membrane, indicating the importance of the multilayer structure. Since the GO membrane exhibits a different interlayer channel (~5 Å) (Fig. 5D) compared with the BP membrane (~4 Å), the intercalation of GO layers into the BP composite membrane establishes a multilevel heterogeneous structure with asymmetric channel size. Such a heterogeneous structure with enhanced retaining and repulsion effect toward the coions could largely enhance the ion separation efficiency and increase the selectivity (evidenced by 81% increase of osmotic potential, Fig. 5E), thus facilitating transmembrane diffusion of counterions (51).

We further investigated the influence of the number of layers of GO on the osmotic energy conversion process. As shown in Fig. 5E and F, increasing the number of GO layers from zero to two results in increased osmotic potential and osmotic current, contributing to increased power density from 1.56 to 3.4 W/m<sup>2</sup>.

The osmotic potential continues to increase upon increasing the number of GO layers from two to four, while the osmotic current decreases substantially. In this regard, although the ion selectivity continues to increase, the transmembrane ion flux will be undermined because the excess GO layers could also confine the ions at the GO/BP interface (52). As a result, the power density decreases to 2.6 W/m<sup>2</sup> (Fig. 5G and *SI Appendix*, Fig. S16). Besides pure electrolyte solutions composed of simple inorganic salts, the composite membrane is also capable of harvesting osmotic energy from a natural water source with a larger salinity ratio (~0.6 M/0.004 M). When we mix natural sea water and river water, the power density achieves a remarkable value of 4.7 W/m<sup>2</sup> (Fig. 5H and *SI Appendix*, Fig. S17) that outperforms most state-of-the-art 2D nanofluidic membranes (16).



## Conclusions

In summary, we observed oxidation promoted osmotic energy conversion in BP membrane. The coexistence of O<sub>2</sub> and water can accelerate the oxidation of BP, creating oxidized phosphorus compounds of diverse valence depending on the O<sub>2</sub> concentration. These functional compounds, especially high-valence (V) ones, serve as charged sites in aqueous electrolyte solution and enhance the transmembrane ion transport, ultimately promoting the power density from 0.5 to 1.6 W/m<sup>2</sup>. Furthermore, by taking inspiration from the natural soil with multilayer architecture, we constructed BP composite membranes by intercalation with GO layers. Different from the previous composite membranes that were formed by simple stacking of mixed 2D materials, our work applied the multilayer 2D architecture for nanofluidic energy conversion. We show that such architecture is superior to the traditional simple stacking 2D membranes with enhanced retaining and repulsion effect toward the coions, largely enhancing the ion separation efficiency. The maximum power output from a mixture of natural river water and sea water can achieve ~4.7 W/m<sup>2</sup>. This work demonstrates that the oxidation of BP can be utilized in nanofluidic osmotic energy conversion, which stands in contrast to applying BP for electronic applications where the ambient stability is a major concern, and reveals its relationship with the power generation process. Such understanding as well as the advanced membrane architecture design may trigger future investigations on BP and other 2D materials toward not only osmotic energy conversion but also other membrane-based applications such as ionic sieving, low-grade heat harvesting, and flow batteries because of their common similarities in core concepts.

## Materials and Methods

**Materials.** BP crystals with a room-temperature resistivity of  $1.5 \pm 0.2 \Omega \text{ cm}^{-1}$  were purchased from Smart Elements (99.998%). Tetra-*n*-butyl-ammonium bisulfate (TBA-HSO<sub>4</sub>), anhydrous propylene carbonate, isopropyl alcohol, and dimethylformamide (DMF) were purchased from Sigma-Aldrich. Anodic inorganic filter membranes with a pore size around 0.2  $\mu\text{m}$  were provided by Whatman. The testing electrolytes including NaCl, KCl, LiCl, MgCl<sub>2</sub>, HCl, and NaOH were all analytical-grade reagents. The sea water was extracted from

the Mediterranean Sea and the river water was extracted from the Elbe River.

**Fabrication of BP and GO-Intercalated BP Membrane.** BP membrane was assembled by vacuum filtration of the BP dispersion in DMF through an anodic membrane filter. After drying in air, a free-standing membrane with good flexibility can be fabricated. To prepare the GO-intercalated BP membrane, few-layer GO was first prepared by the well-developed Hummers method. Then, the multilayer membrane was prepared by sequential filtration of BP and GO dispersion. The thickness of each layer could be precisely regulated through the dosage of the dispersion. The following shows the composition of the multilayer membrane: BP/(GO/BP)<sub>1</sub>: 3.75  $\mu\text{m}$  BP/0.5  $\mu\text{m}$  GO/3.75  $\mu\text{m}$  BP; BP/(GO/BP)<sub>2</sub>: 2.33  $\mu\text{m}$  BP/0.5  $\mu\text{m}$  GO/2.33  $\mu\text{m}$  BP/0.5  $\mu\text{m}$  GO/2.33  $\mu\text{m}$  BP; BP/(GO/BP)<sub>3</sub>: 1.63  $\mu\text{m}$  BP/0.5  $\mu\text{m}$  GO/1.63  $\mu\text{m}$  BP/0.5  $\mu\text{m}$  GO/1.63  $\mu\text{m}$  BP/0.5  $\mu\text{m}$  GO/1.63  $\mu\text{m}$  BP; BP/(GO/BP)<sub>4</sub>: 1.2  $\mu\text{m}$  BP/0.5  $\mu\text{m}$  GO/1.2  $\mu\text{m}$  BP/0.5  $\mu\text{m}$  GO/1.2  $\mu\text{m}$  BP/0.5  $\mu\text{m}$  GO/1.2  $\mu\text{m}$  BP/0.5  $\mu\text{m}$  GO/1.2  $\mu\text{m}$  BP. The total thickness of the hybrid membrane is uniformly set to ~8  $\mu\text{m}$ . To fabricate the contrast sample, certain amounts of GO and BP dispersions were mixed beforehand, then the BP/GO mixture was sonicated for 15 min and assembled by the same vacuum filtration method. The water treatment was performed by immersing the as-prepared membranes in DI water with different O<sub>2</sub> concentration for different period of time.

**Electrochemical Testing.** To measure the transmembrane ion transport, the membrane was clamped in a two-compartment electrochemical cell. The ionic current was measured with an electrochemical workstation (CHI) through a pair of Ag/AgCl electrodes. The testing membrane area (i.e., area used to evaluate the performance) was about  $3 \times 10^4 \mu\text{m}^2$ . The osmotic energy conversion behavior was evaluated by connecting the system to an external circuit with an adjustable resistance (Reichelt Elektronik). Ultrapure water ( $18.2 \text{ M}\Omega \cdot \text{cm}^{-1}$ ) was used for preparing ionic solutions.

**Data Availability.** All data are included in the paper and *SI Appendix*. *SI Appendix* contains methods, associated protocols, and electrochemical and physical characterization data that were used to produce and support the results in this paper (*SI Appendix*, Figs. S1–S17).

**ACKNOWLEDGMENTS.** Z.Z. acknowledges the support of the Alexander von Humboldt Foundation. This work was financially supported by the European Union's Horizon 2020 research and innovation programme under Grant 881603, the European Science Foundation, and Coordination Networks: Building Blocks for Functional Systems (SPP1928).

1. A. R. Koltonow, J. Huang, IONIC TRANSPORT. Two-dimensional nanofluidics. *Science* **351**, 1395–1396 (2016).
2. L. Jubin, A. Poggiali, A. Siria, L. Bocquet, Dramatic pressure-sensitive ion conduction in conical nanopores. *Proc. Natl. Acad. Sci. U.S.A.* **115**, 4063–4068 (2018).
3. L. Wang et al., Fundamental transport mechanisms, fabrication and potential applications of nanoporous atomically thin membranes. *Nat. Nanotechnol.* **12**, 509–522 (2017).
4. R. R. Nair, H. A. Wu, P. N. Jayaram, I. V. Grigorieva, A. K. Geim, Unimpeded permeation of water through helium-leak-tight graphene-based membranes. *Science* **335**, 442–444 (2012).
5. S. Qin et al., High and stable ionic conductivity in 2D nanofluidic ion channels between boron nitride layers. *J. Am. Chem. Soc.* **139**, 6314–6320 (2017).
6. Y. Kang, Y. Xia, H. T. Wang, X. W. Zhang, 2D laminar membranes for selective water and ion transport. *Adv. Funct. Mater.* **29**, 1902014 (2019).
7. C. Cheng, G. Jiang, G. P. Simon, J. Z. Liu, D. Li, Low-voltage electrostatic modulation of ion diffusion through layered graphene-based nanoporous membranes. *Nat. Nanotechnol.* **13**, 685–690 (2018).
8. M. Deng, K. Kwac, M. Li, Y. Jung, H. G. Park, Stability, molecular sieving, and ion diffusion selectivity of a lamellar membrane from two-dimensional molybdenum disulfide. *Nano Lett.* **17**, 2342–2348 (2017).
9. Q. Yang et al., Ultrathin graphene-based membrane with precise molecular sieving and ultrafast solvent permeation. *Nat. Mater.* **16**, 1198–1202 (2017).
10. J. Abraham et al., Tunable sieving of ions using graphene oxide membranes. *Nat. Nanotechnol.* **12**, 546–550 (2017).
11. B. Mi, Materials science. Graphene oxide membranes for ionic and molecular sieving. *Science* **343**, 740–742 (2014).
12. L. Chen et al., Ion sieving in graphene oxide membranes via cationic control of interlayer spacing. *Nature* **550**, 380–383 (2017).
13. J. Feng et al., Single-layer MoS<sub>2</sub> nanopores as nanopower generators. *Nature* **536**, 197–200 (2016).
14. A. Siria, M. L. Bocquet, L. Bocquet, New avenues for the large-scale harvesting of blue energy. *Nat. Rev. Chem.* **1**, 91 (2017).
15. A. Aliprandi, D. Pakulski, A. Ciesielski, P. Samori, Punctured two-dimensional sheets for harvesting blue energy. *ACS Nano* **11**, 10654–10658 (2017).
16. Z. Zhang et al., Mechanically strong MXene/Kevlar nanofiber composite membranes as high-performance nanofluidic osmotic power generators. *Nat. Commun.* **10**, 2920 (2019).
17. L. Ding et al., Oppositely charged Ti<sub>3</sub>C<sub>2</sub>T<sub>x</sub> MXene membranes with 2D nanofluidic channels for osmotic energy harvesting. *Angew. Chem. Int. Ed.* **132**, 1–9 (2020).
18. Y. Feng, W. Zhu, W. Guo, L. Jiang, Bioinspired energy conversion in nanofluidics: A paradigm of material evolution. *Adv. Mater.* **29**, 1702773 (2017).
19. X. Ling, H. Wang, S. Huang, F. Xia, M. S. Dresselhaus, The renaissance of black phosphorus. *Proc. Natl. Acad. Sci. U.S.A.* **112**, 4523–4530 (2015).
20. J. Kang et al., Stable aqueous dispersions of optically and electronically active phosphorene. *Proc. Natl. Acad. Sci. U.S.A.* **113**, 11688–11693 (2016).
21. M. Qiu et al., Novel concept of the smart NIR-light-controlled drug release of black phosphorus nanostructure for cancer therapy. *Proc. Natl. Acad. Sci. U.S.A.* **115**, 501–506 (2018).
22. Z. Hu et al., Water-catalyzed oxidation of few-layer black phosphorus in a dark environment. *Angew. Chem. Int. Ed. Engl.* **56**, 9131–9135 (2017).
23. D. Hanlon et al., Liquid exfoliation of solvent-stabilized few-layer black phosphorus for applications beyond electronics. *Nat. Commun.* **6**, 8563 (2015).
24. W. Luo et al., Surface chemistry of black phosphorus under a controlled oxidative environment. *Nanotechnology* **27**, 434002 (2016).
25. Y. Abate et al., Recent progress on stability and passivation of black phosphorus. *Adv. Mater.* **30**, e1704749 (2018).
26. J. D. Wood et al., Effective passivation of exfoliated black phosphorus transistors against ambient degradation. *Nano Lett.* **14**, 6964–6970 (2014).
27. J. Cui et al., Ultrafast Li<sup>+</sup> diffusion kinetics of 2D oxidized phosphorus for quasi-solid-state bendable batteries with exceptional energy densities. *Chem. Mater.* **31**, 4113–4123 (2019).
28. P. Nakhani et al., Revealing molecular-level surface redox sites of controllably oxidized black phosphorus nanosheets. *Nat. Mater.* **18**, 156–162 (2019).
29. J. Sun et al., A phosphorene-graphene hybrid material as a high-capacity anode for sodium-ion batteries. *Nat. Nanotechnol.* **10**, 980–985 (2015).
30. Y. Zhang et al., Wet-chemical processing of phosphorus composite nanosheets for high-rate and high-capacity lithium-ion batteries. *Adv. Energy Mater.* **6**, 1502409 (2016).

31. P. Yasaei *et al.*, Stable and selective humidity sensing using stacked black phosphorus flakes. *ACS Nano* **9**, 9898–9905 (2015).
32. M. B. Erande, M. S. Pawar, D. J. Late, Humidity sensing and photodetection behavior of electrochemically exfoliated atomically thin-layered black phosphorus nanosheets. *ACS Appl. Mater. Interfaces* **8**, 11548–11556 (2016).
33. B. Tian *et al.*, Facile bottom-up synthesis of partially oxidized black phosphorus nanosheets as metal-free photocatalyst for hydrogen evolution. *Proc. Natl. Acad. Sci. U.S.A.* **115**, 4345–4350 (2018).
34. J. Zhao *et al.*, Liquefaction of water on the surface of anisotropic two-dimensional atomic layered black phosphorus. *Nat. Commun.* **10**, 4062 (2019).
35. X. Liu *et al.*, Power generation by reverse electrodialysis in a single-layer nanoporous membrane made from core-rim polycyclic aromatic hydrocarbons. *Nat. Nanotechnol.* **15**, 307–312 (2020).
36. S. Yang *et al.*, A delamination strategy for thinly layered defect-free high-mobility black phosphorus flakes. *Angew. Chem. Int. Ed. Engl.* **57**, 4677–4681 (2018).
37. X. Hou, Smart gating multi-scale pore/channel-based membranes. *Adv. Mater.* **28**, 7049–7064 (2016).
38. P. Gao *et al.*, Distinct functional elements for outer-surface anti-interference and inner-wall ion gating of nanochannels. *Nat. Commun.* **9**, 4557 (2018).
39. G. Pérez-Mitta, W. A. Marmisollé, C. Trautmann, M. E. Toimil-Molares, O. Azzaroni, Nanofluidic diodes with dynamic rectification properties stemming from reversible electrochemical conversions in conducting polymers. *J. Am. Chem. Soc.* **137**, 15382–15385 (2015).
40. K. Raidongia, J. Huang, Nanofluidic ion transport through reconstructed layered materials. *J. Am. Chem. Soc.* **134**, 16528–16531 (2012).
41. R. Fan, S. Huh, R. Yan, J. Arnold, P. Yang, Gated proton transport in aligned mesoporous silica films. *Nat. Mater.* **7**, 303–307 (2008).
42. S. Hong *et al.*, Scalable graphene-based membranes for ionic sieving with ultrahigh charge selectivity. *Nano Lett.* **17**, 728–732 (2017).
43. J. J. Shao, K. Raidongia, A. R. Koltonow, J. Huang, Self-assembled two-dimensional nanofluidic proton channels with high thermal stability. *Nat. Commun.* **6**, 7602 (2015).
44. T. Li *et al.*, A nanofluidic ion regulation membrane with aligned cellulose nanofibers. *Sci. Adv.* **5**, eaau4238 (2019).
45. K. Xiao, P. Giusto, L. Wen, L. Jiang, M. Antonietti, Nanofluidic ion transport and energy conversion through ultrathin free-standing polymeric carbon nitride membranes. *Angew. Chem. Int. Ed. Engl.* **57**, 10123–10126 (2018).
46. X. B. Zhu *et al.*, Unique ion rectification in hypersaline environment: A high-performance and sustainable power generator system. *Sci. Adv.* **4**, eaau1665 (2018).
47. R. Li, J. Jiang, Q. Liu, Z. Xie, J. Zhai, Hybrid nanochannel membrane based on polymer/MOF for high-performance salinity gradient power generation. *Nano Energy* **53**, 643–649 (2018).
48. A. Siria *et al.*, Giant osmotic energy conversion measured in a single transmembrane boron nitride nanotube. *Nature* **494**, 455–458 (2013).
49. T. Zhang *et al.*, Degradation chemistry and stabilization of exfoliated few-layer black phosphorus in water. *J. Am. Chem. Soc.* **140**, 7561–7567 (2018).
50. S. Ling *et al.*, Design and function of biomimetic multilayer water purification membranes. *Sci. Adv.* **3**, e1601939 (2017).
51. H. C. Zhang *et al.*, Ultrafast selective transport of alkali metal ions in metal organic frameworks with subnanometer pores. *Sci. Adv.* **4**, eaaq0066 (2018).
52. Z. Zhu, D. Wang, Y. Tian, L. Jiang, Ion/molecule transportation in nanopores and nanochannels: From critical principles to diverse functions. *J. Am. Chem. Soc.* **141**, 8658–8669 (2019).